AADE-23-NTCE-014

A Coupled Geomechanics-Reservoir Simulation Workflow to Estimate the Optimal Well-Spacing in the Wolfcamp Formation in Lea County

Dung Bui, Tan Nguyen, and Hyunsang Yoo, New Mexico Institute of Mining and Technology

Abstract

This paper aims to present a workflow to estimate optimal well-spacing in the Wolfcamp A formation in Lea County, New Mexico. The failure to predict optimal well-spacing could lead to well communication, which is the root cause of low hydrocarbon recovery. In such scenarios, a coupled geomechanics-reservoir model can provide a handy approach for well-spacing optimization.

First, the geomechanical properties of the reservoir obtained from a mechanical earth model (MEM) were coupled with a 3D geological model to estimate the fracture propagation of the existing (parent) well. The fracture geometry of the parent well was validated by history matching the production data. Then, the matched model was used to simulate fracture propagation of the infill (child) well. Simulation results show that fracture geometry, fracture permeability, and relative permeability in the fractured zone are the most sensitive factors in the history matching. The estimated fracture geometry of the parent well ranges from 150 to 900 ft half-length and 100 to 400 ft height for each fracture stage. Spacing analysis between two wells based on the coupled geomechanics-reservoir model was conducted from 600 to 1300 ft with 50-ft increment. It provides an optimal spacing to avoid fracture hit and maximize the ultimate recovery.

The novelty of the proposed approach is the ability to simulate fracture growth of the child well in 3D using the coupled geomechanics model. Based on the fracture propagation estimation of both wells, optimizing the total oil recovery of both wells is feasible.

Introduction

According to U.S. Energy Information Administration (EIA), the Permian Basin of West Texas and Southeast New Mexico has produced hydrocarbon for about 100 years and supplied more than 35.6 billion barrels of oil and about 125 trillion cubic feet of natural gas as of January 2020. EIA estimated remaining proven reserves in the Permian Basin exceed 11 billion barrels of oil and 46 trillion cubic feet (Tcf) of natural gas, making it one of the largest hydrocarbon-producing basins in the U.S. and the world (EIA, 2020). The Permian Basin is comprised of several sub-basins and platforms; three main sub-divisions include the Midland Basin, Central Basin Platform, and the Delaware Basin. It also contains many formations within the three main sub-divisions.

In 2018, the U.S. Geological Survey (USGS) reported that the Delaware Basin assessment of the Wolfcamp Shale and Bone Spring Formation is more than two times larger than that of the Midland Basin, making it one of the most productive basins in the U.S. The Wolfcamp formation is located beneath the Third Bone Spring formation and divided into four sections, or benches, known as Wolfcamp A, B, C, and D. Most of the current drilling activities in the Delaware Basin targets Upper Wolfcamp (A and B benches) rather than Lower Wolfcamp (C and D benches), which is more natural gas prone and more mature (EIA, 2020). EIA (2020)'s analysis of well log suggested that porosity of the Wolfcamp formation varies between 2% and 12% and averages 6%, but all subsections have very low permeability at an average of less than a few millidarcies. Low porosity and low permeability reservoirs require horizontal drilling and multistage hydraulic fracturing.

One of the difficulties of the hydraulic fracture technique is to precisely predict the propagation of fractures (Michael, 2022). Due to the high heterogeneity of rock properties, it is very challenging to get a reliable prediction of fracture geometry. As of 2021, there are more than 1400 horizontal wells drilled in the Wolfcamp formation but it is still not clear what is the optimal well spacing in the Delaware Basin. Failure in predicting fracture propagation could lead to well communication and fracture hit. In many cases, they are the root causes of low hydrocarbon recovery (King et al. 2017; Rezaei et al. 2021). Several techniques and tools are implemented in the industry to map the stimulated reservoir volume, to quantify the well communication, and to monitor propagating fractures. According to Khodabakhshnejad (2019), some of the most popular tools used are: microseismic monitoring of fracture events (Cipolla et al. 2010; Neuhaus et al. 2014; McKenna et al. 2016; Trowbridge et al. 2017) and the wellhead and downhole pressure monitoring of nearby wells (Sani et al. 2015; Lehmann et al. 2016; Liang et al. 2017; King et al. 2017). Other studies optimize well spacing in the Wolfcamp formation in Delaware

Basin using the data analytics approach (Alzahabi et al. 2021), or whole pad estimated ultimate recovery (EUR) versus the number of wells in a section (Liang et al. 2017, Cao et al. 2017). However, the input data for above techniques are not always available. For instance, field data is insufficient, real-time monitoring and measurement are too expensive, etc. In such cases, reservoir simulation can provide an economical and handy approach for the prediction of fracture growth, avoiding well communication, and forecasting total production. Some recent simulation studies are focusing on the neighborhood basins and formations such as Midland Basin (Xiong et al. 2017; Zhu et al. 2017; Park and Janova 2020) and Second Bone Spring (Hefner and Davudov 2019). Due to the different distribution of rock properties, fluid properties, and rock-fluid function between Delaware and Midland Basin, fracture geometries of the two basins could be very different. In addition, there is no available research that has conducted well spacing analysis based on the fracture propagation of the infill well itself in a 3D model. Therefore, a coupled geomechanics-reservoir simulation to effectively predict fracture propagations of parent and child wells and optimize well spacing in the Delaware Basin is needed. This paper provides a step-by-step workflow to construct the model and conduct the well spacing analysis to achieve the optimal spacing, therefore enhancing EUR.

Workflow

The workflow to construct the coupled geomechanics-reservoir model consists of three steps including (1) build a geological model for the formation of interest, (2) estimate elastic properties and in-situ stress of the rock formation by a MEM to couple with reservoir simulation, and (3) simulate fracture propagation of the parent well and history match the production data. Then, the matched model is used to conduct well spacing analysis with the simulated fracture propagations of the infill well.

Step 1 – Build the geological model of the formation

This research focuses on building the geological model for one section of Wolfcamp A formation (approximately one-by-one mile) in the Delaware Basin in Lea County. Log data of four vertical wells (data points) in the location were collected from Enverus DrillingInfo Inc. Longitudes and latitudes of the four data points along with the formation tops of Wolfcamp A and B formations were imported to Petrel (a commercial reservoir simulation software developed by Schlumberger). Using a well correlation process in Petrel, a 3D structural model representing the Wolfcamp A formation was successfully constructed. A producing fractured horizontal well (parent well) is located in the simulation by inputting the survey data to the structural model. Fig. 1 shows the structural map of the Wolfcamp A formation with four data points and the parent well.

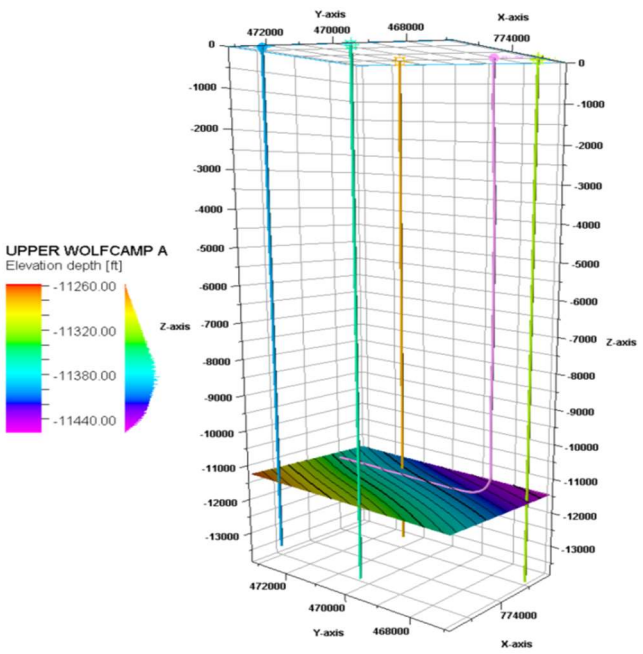

Figure 1 – Structural map of the formation of interest

After the construction of the structural model, reservoir properties of the formations of interest need to be populated in the model. A detailed discussion of the construction of the static model and reservoir characterization in Petrel is presented by Koray et al. 2023a and Koray et al. 2023b. To calculate total porosity of the formations, the cross-plot technique relying on a combination of the neutron porosity and bulk density is applied (Alberty 1994). In this technique, a cross-plot with the neutron reading marked on the horizontal axis and bulk density on the vertical axis is used with the appropriate mud type (fresh or salt). This method is performed using Techlog (a Schlumberger's log analysis software) to obtain the continuous porosity curves to be used in Petrel. Gamma ray (GR) logs also suggest that the Wolfcamp A formation contains a considerable volume of shale, so effective porosity of the formation is calculated by Eq. (1) as follows:

$$\varphi_e = \varphi_T - V_{sh} * \varphi_{sh} \quad (1)$$

where φ_T is total porosity, φ_e is effective porosity, V_{sh} is volume of shale, and φ_{sh} is shale porosity. Shale porosity is calculated in Techlog by Eq. (2) as follows (Techlog, 2020):

$$\varphi_{sh} = \frac{\rho_{ma} - \rho_{sh}}{\rho_{ma} - \rho_f} \quad (2)$$

where ρ_{ma} is density of rock matrix, g/cm^3; ρ_{sh} is density of shale, g/cm^3; ρ_f is fluid density, g/cm^3. Shale volume is calculated from GR log using Larionov correlation for older rock as Wolfcamp is considered "older" in age. Eqs. (3) and (4) present the Larionov correlation that Techlog uses to calculate shale volume based on GR log data.

$$GR_{index} = \frac{GR - GR_{matrix}}{GR_{shale} - GR_{matrix}} \quad (3)$$

$$V_{sh} = 0.33 * (2^{2*GR_{index}} - 1) \quad (4)$$

where GR is gamma-ray data, GR_{matrix} is gamma-ray of a clean reservoir having no shale, GR_{shal} is gamma-ray of a 100% shale zone. Bulk density (ρ_b), neutron porosity (φ_N), and shale

volume (V_{sh}) are the inputs to calculate effective porosity in Techlog. Fig. 2 shows the plots of the calculated effective porosity from four vertical wells in Techlog.

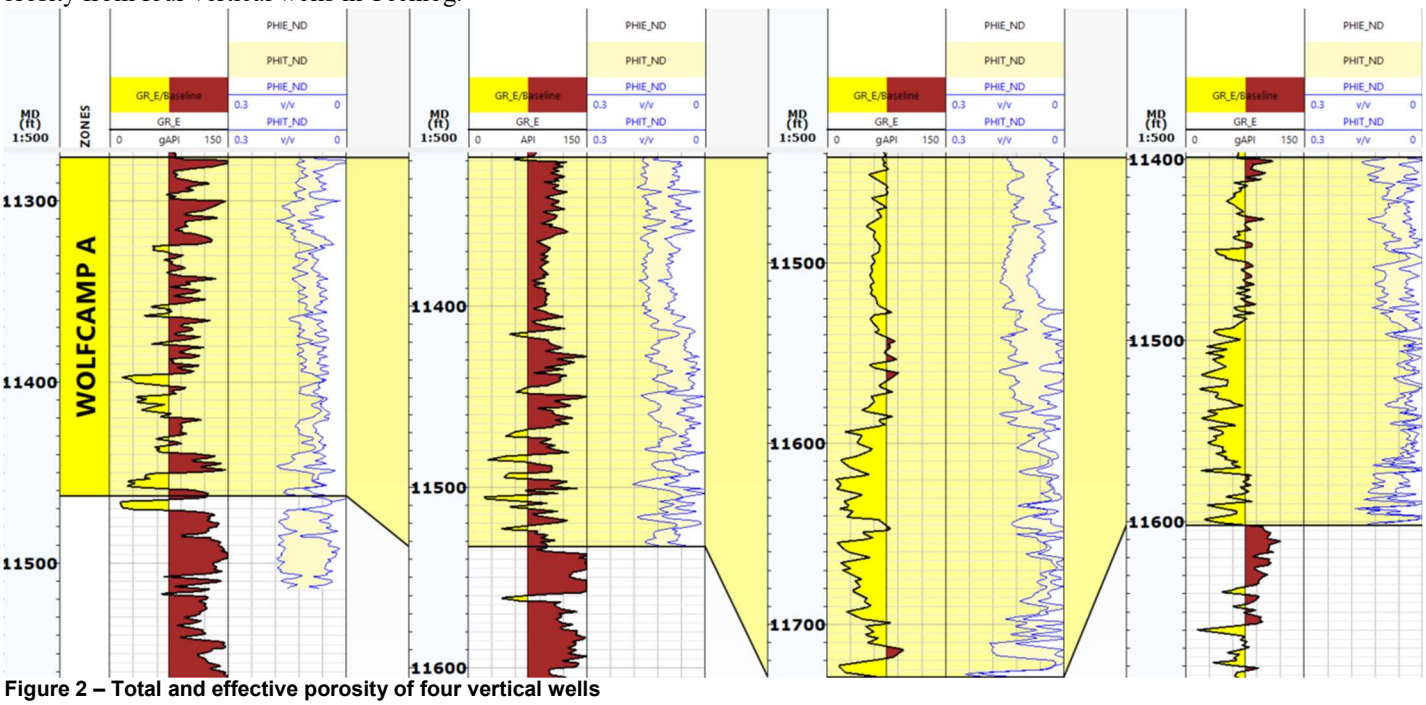

Figure 2 – Total and effective porosity of four vertical wells

Next, the effective porosity of Wolfcamp A formation is populated in Petrel as shown in Fig. 3, with the range from 1% to 9% and most of the values falling into the range of 2% and 6%. This result is very similar to the EIA's report for the porosity of Wolfcamp A in 2020 (varying from 2% to 12% and the average of 6%).

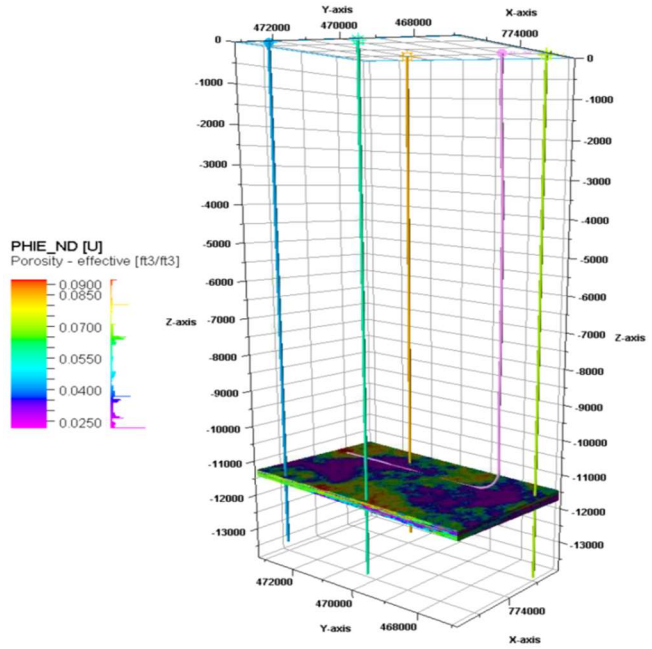

Figure 3 – Effective porosity map of the formation

The permeability of the formation is correlated using published data (Hefner 2020) in Wolfcamp A-XY formation in Eddy County. The correlation is achieved by an exponent regression as shown in Eq. (5):

$$k = 3 * 10^{-6} * \exp(84.859 * \varphi_e) \quad (5)$$

where k is permeability, mD; φ_e is effective porosity.

Using the permeability versus porosity correlation, the permeability of the formation is populated in Petrel as shown in Fig. 4. The permeability distribution ranges from 18 nD to 7550 nD. This result is consistent with published data where other authors show the range from 1 nD to 5500 nD (Ramirez et al. 2020) and from 2.75 nD to 8850 nD (Jones 2019) in the Upper Wolfcamp formation in Delaware Basin.

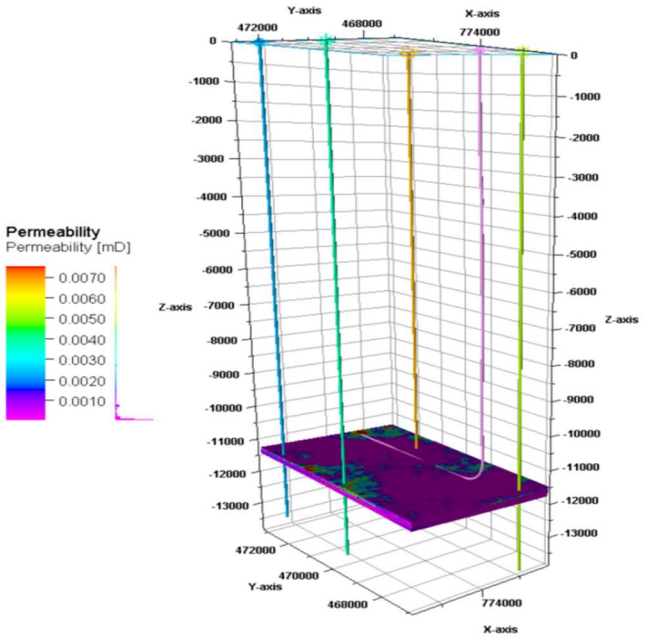

Figure 4 - Permeability map of the formation

Step 2 – MEM for geomechanical properties estimation

To obtain required geomechanical propterties for the geomechanics-reservoir coupled model, the MEM needs to be performed to obtain the elastic properties of the rock, rock strength, and in-situ stress, which is calibrated by instantaneous shut-in pressure (ISIP) data (Dvory and Zoback, 2021). Pore pressure prediction is performed using the Eaton method (1975) and calibrated with published DST data in Lea County (Luo et al. 1994; Nguyen et al. 2023). Log data, including bulk density, compressional, and shear slowness, are collected from a vertical well 16 miles away in Lea County. The complete 1D MEM modeling scheme is presented in Fig. 5.

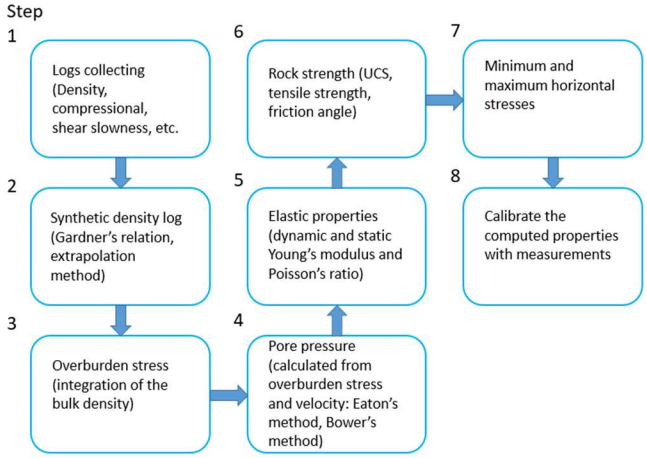

Figure 5 - Step by step MEM workflow for computing material properties and horizontal stresses (after Abedin and Henk 2020)

The MEM workflow starts with the overburden stress's calculation based on bulk density log. The overburden stress is the integration of the bulk density from the surface to the depth of interest and can be expressed in Eq. (6) as follows:

$$\sigma_V = g\int_0^{TVD} \rho_{b(z)} d_z \tag{6}$$

where σ_V is the vertical stress, $\rho_{b(z)}$ is the bulk density at depth z below the earth's surface, and g is the gravitational acceleration. In case of missing bulk density data, Gardner's correlation (1974) can be used to generate a synthetic density curve from compressional velocity, V_p, as follows:

$$\rho_b = \alpha V_p^{\beta} \tag{7}$$

Fitting parameter α and β are adjusted to obtain the best fit between the calculated density curve and the bulk density log (Nguyen et al. 2015).

Pore pressure is not only a key parameter required to determine effective stresses in MEM but also a must to ensure the safety and efficiency of the drilling process (Nguyen et al. 2018). Various methods and correlations have been put forward to get a pore pressure profile. The two most popular ones are Eaton's method (1975) and Bower's method (1995). Eaton (1975) stated that since rocks are more resistive to electrical current than is formation water, a well compacted shale containing less water is more resistive than a less compacted shale containing more water. Also, a sequence of normally compacted sediments should have a normally increasing resistivity trend. Thus, any resistivity decrease from the normal trend indicates the presence of abnormally high-pressure zone. A similar idea was used in conjunction for the pore pressure gradient with sonic log travel-time departure from normal travel-time. Eaton's method to calculate pore pressure can be expressed in Eq. (8) as follows:

$$P_p = \sigma_V - (\sigma_V - P_n) * \left(\frac{\Delta t_n}{\Delta t}\right)^n \tag{8}$$

where P_p is pore pressure; P_n is normal hydrostatic pressure; Δt_n is compressional slowness at normal pressure; n is Eaton exponent and equal to 3.0.

Elastic properties required for geomechanical modeling such as Young's modulus, Poisson's ratio, shear and bulk moduli can be computed at first from log data for their dynamic properties. Material in this research is assumed to be continuous, homogeneous, isotropic, linear, and elastic (CHILE). Then, they are transferred to static properties by empirical correlations. The static properties can be crosschecked at calibration points if lab tests on cores are available. Many empirical correlations are available to calculate such static properties from the dynamic values, e.g., Bradford (1998), Morales (1993), Canady (2011). In all calculations of dynamic properties, shear wave interval transit time is required.

Rock strength parameters (UCS, tensile strength, friction angle) are estimated indirectly by using various correlations with elastic properties, e.g., Coates-Denoo (1981), Plumb (1994), Bradford (1998).

Horizontal stresses can be estimated based on a poro-elastic approach considering tectonic strains as shown in Eqs. (9) and (10) as follows:

$$\sigma_h = \frac{\nu}{1-\nu}\sigma_V - \frac{\nu}{1-\nu}\alpha P_p + \alpha P_p + \frac{E}{1-\nu^2}\varepsilon_h + \frac{\nu E}{1-\nu^2}\varepsilon_H \tag{9}$$

$$\sigma_H = \frac{\nu}{1-\nu}\sigma_V - \frac{\nu}{1-\nu}\alpha P_p + \alpha P_p + \frac{E}{1-\nu^2}\varepsilon_H + \frac{\nu E}{1-\nu^2}\varepsilon_h \tag{10}$$

where σ_h and σ_H are minimum and maximum horizontal stress magnitudes, respectively; E is Young's modulus; ν is Poisson's ratio; α is Biot constant; ε_h and ε_H are the minimum and maximum horizontal strain magnitudes. Since tectonic strains are not available, σ_h is calibrated with diagnostic fracture injection test (DFIT) data from the fracture reports and σ_H is computed from ratio with σ_h. The calibration of the in-situ stresses can also be performed utilizing time-lapse vertical seismic profile data assisted with machine learning workflow (Ampomah et al. 2022). The stress ratio between σ_H and σ_h is obtained from Eqs. (11) and (12) as follows (Snee and Zoback, 2018):

$$A_\varphi = (n + 0.5) + (-1)^n(\varphi - 0.5) \tag{11}$$

$$\varphi = \frac{\sigma_H - \sigma_h}{\sigma_V - \sigma_h} \tag{12}$$

where A_φ parameter is faulting regime varying from 0 to 1.5 corresponding with radial normal faulting, normal faulting (NF),

and strike-slip faulting (SS); n is 0 for NF, 1 for SS, and 2 for reverse faulting, respectively. According to Snee and Zoback (2018), A and n in Lea County are 0.5 and 0, respectively, giving a stress ratio between σ_H and σ_h of 1.1.

The results of MEM calculation for overburden pressure, pore pressure, Young's modulus (E), Poisson's ratio (ν), unconfined compressive strength (UCS), and minimum and maximum horizontal stresses is shown in Fig. 6.

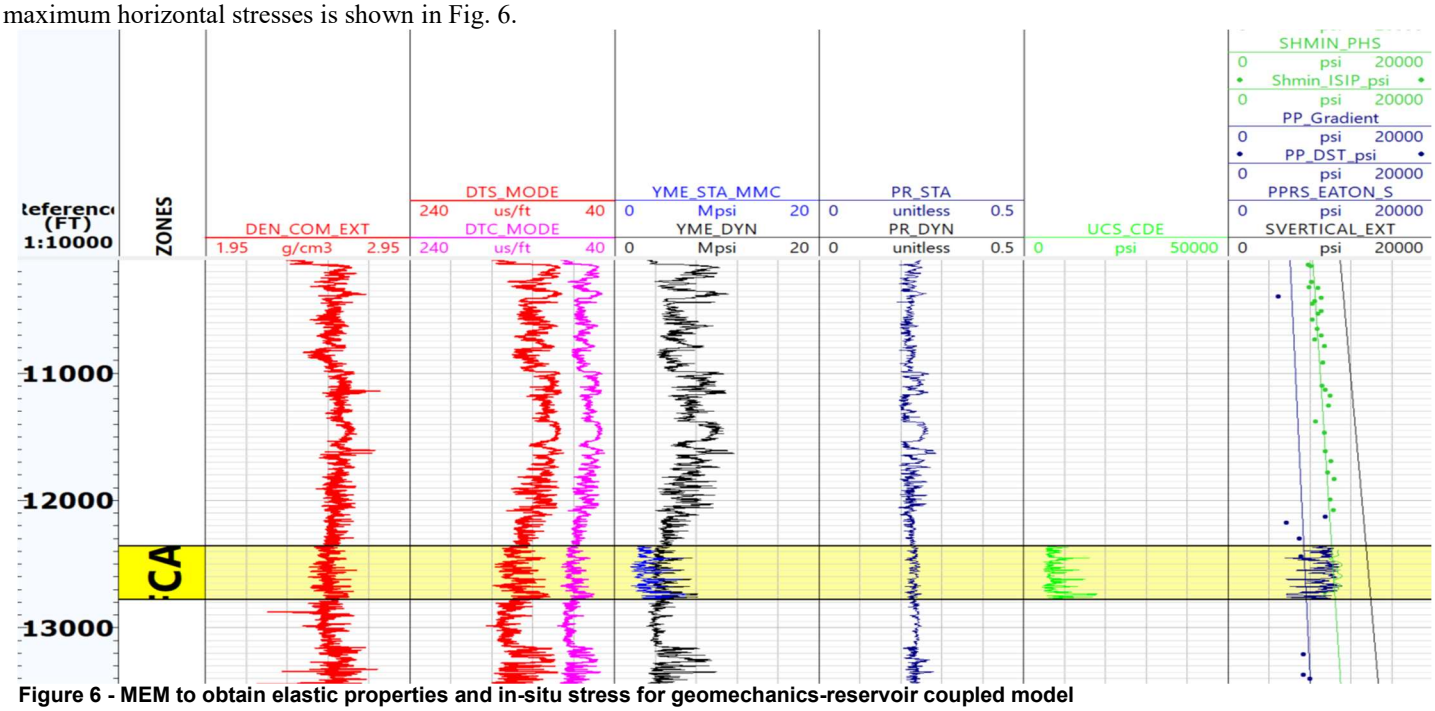

Figure 6 - MEM to obtain elastic properties and in-situ stress for geomechanics-reservoir coupled model

From the results of MEM, estimated pore pressure, minimum horizontal stress, and overburden stress gradients of 0.62, 0.82, and 1.09 psi/ft, respectively, are implemented in the geomechanics-reservoir coupled model.

Step 3 – Simulation of parent well's fracture propagation

The fundamentals of simulating hydraulic fracture propagation in a coupled geomechanics-reservoir model are based on the two sets of fluid flow and deformation equations (Tran et al. 2008). The two sets of equations: one for fluid flow in porous media and another for rock deformation are well-integrated in Computer Modelling Group (CMG) reservoir simulator. The fluid-flow equations include conservation of mass and energy; the basic equations for rock deformation include deformation, strain, and stress. In the iterative coupling approach, the two sets of equations are solved separately. At a certain time-step, pore pressure in the reservoir flow simulator is computed first, then sent to the geomechanics simulator, where displacement, strain, and stress are computed. The solution from the geomechanics module is then passed back to the reservoir simulation via two coupling variables – porosity and permeability. These two coupling variables are used to recompute a new pressure distribution in the reservoir simulator. Again, this new pressure is resent to the geomechanics module to recalculate deformation, strain, and stress. The above process is continued until an acceptable error tolerance is achieved (Tran et al. 2009a).

The initiation of a hydraulic fracture is based on the tensile fracture mode, which is the most common failure type in hydraulic fracturing. At the beginning, the in-situ stress state is not under the failure condition as shown in Eq. (13) as follows:

$$\sigma_h' = \sigma_h - \mathrm{P} > \mathrm{T}_0 \tag{13}$$

where σ_h and σ_h' are the total and effective minimum horizontal stress, respectively, P is the pore pressure, and T_0 is the tensile strength of the rock. When fracture fluid is injected into the formation, it increases the pore pressure, therefore decreasing effective stress. If the pore pressure increases to a certain value that σ_h' drops below the rock tensile strength, the failure criterion is satisfied so hydraulic fracture is initiated and propagates perpendicular to the minimum horizontal stress direction (Bui et al. 2022). By applying the described geomechanics coupled model, CMG is able to simulate the fracture propagation of the parent well using the fracture schedule from the field data. Each stage was pumped with 75 barrels per minute (bpm) of slick water in 106 minutes. There were 21 fracture stages simulated by CMG for the parent well. The results and discussion section presents the fracture geometry of the parent well in more detail.

After the simulation of fracture propagation, the pumps shut and the fracture permeability under downhole condition is computed by CMG. Once the pumps shut, fractures start to close under the closure stress of the formation. To account for the proppant permeability behavior under the closure stress, a fracture permeability based on the modification of the Barton-Bandis model (1985) is implemented in CMG (Tran et al. 2009b; Bui et al. 2022) as shown in Fig. 7.

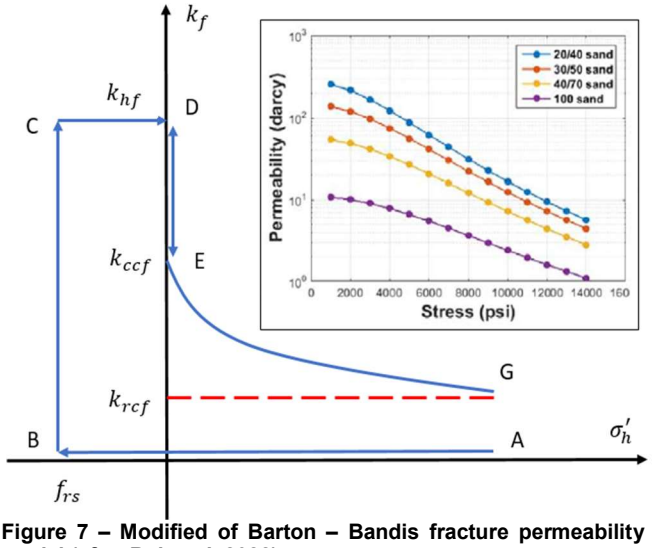

Figure 7 – Modified of Barton – Bandis fracture permeability model (after Bui et al. 2022)

Effective minimum horizontal stress (σ'_h) is located at point A at the beginning. When σ'_h decreases from its initial value to tensile stress (f_{rs}) of the rock at point B, fractures initiate and the stimulated zones have the fracture permeability equal to the proppant permeability (k_{hf}). As soon as pumps stop, fractures begin to close. The fracture permeability drops from k_{hf} at point D to closure permeability (k_{ccf}) at point E as σ'_h increases from point C to point D. With the mechanical support of proppant, fractures do not close entirely, but they will lose their conductivities and be forced to close gradually (Huang et al. 2019). As fractures close and proppant-pore-structures compact, the effective permeability of the stimulated zone is decreased to a lower value called residual fracture permeability (k_{rcf}) at point G. A similar phenomenon of stress dependent permeability happened in the rock matrix was also mentioned by Nguyen et al. 2020, where the increase of effective stress due to depletion reduces the formation permeability in unconventional reservoirs. Therefore, the residual proppant permeability could be very limited and different from the original proppant permeability.

Simulation setup

The reservoir simulation covers an approximate area of 3450-ft by 6300-ftconsisting of the active oil production well (parent well) with 21 hydraulic fracture stages. CMG software was used to simulate the hydraulic fractures and flows in the natural fractured shale formation. The formation depth is at 11258 ft (3420-m) with 3450 ft (1052-m) on the x-axis, 6300 ft (1920-m) on the y-axis, and approximately 220 ft (67-m) thickness on the z-axis. The model is discretized by 69 x 126 x 10 grid blocks. The grid sizes in x and y-direction are 50-ft and the z-direction is about 22-ft each layer. Table 1 shows the summary of reservoir properties as follows:

Table 1. Reservoir properties

Properties	Input
Top formation depth	11258 ft (3420-m)
Reservoir porosity	2 – 9%
Reservoir permeability	18 – 7500 nD
Average pore pressure	7122 psi
Reservoir temperature	169 F
Young modulus, E	3.5 Mpsi
Poisson's ratio, ν	0.25
σ_V gradient	1.09 psi/ft
σ_h gradient	0.82 psi/ft
Bubble point pressure	3,546 psi
Oil API	43.5
Gas gravity (air = 1)	0.82
Gas oil ratio	1,400 scf/stb
Number of grid blocks	69 x 126 x 10
Grid sizes	dx = dy = 50 ft; dz ≅ 22 ft

Figs. 8 and 9 show the porosity and permeability of the reservoir in CMG, respectively, and existing horizontal well in the Wolfcamp A formation.

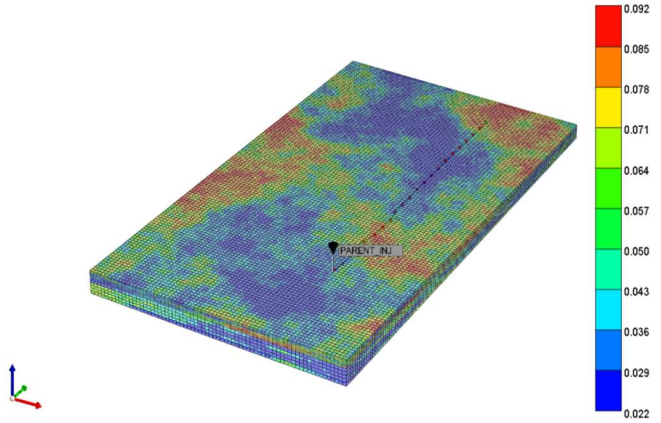

Figure 8 – Porosity distribution of the formation

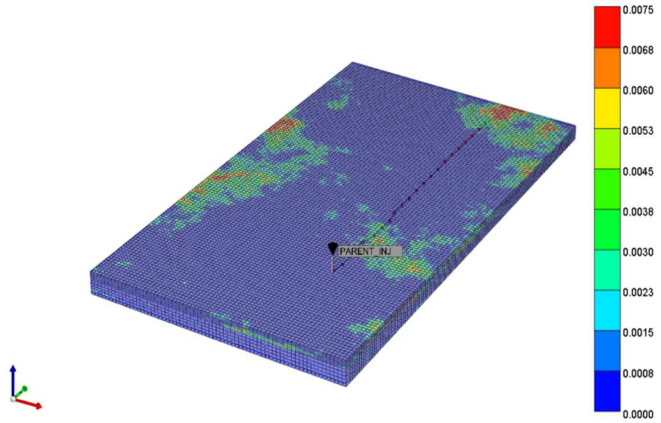

Figure 9 – Permeability distribution of the formation

To simulate multiphase flow in the reservoir, relative permeability curves of water-oil and gas-liquid systems need to be incorporated into the model. Various shale samples were measured by Ojha et al. (2017a and 2017b) to obtain relative permeability estimations for the Wolfcamp shale formation as shown in Fig. 10 as follows:

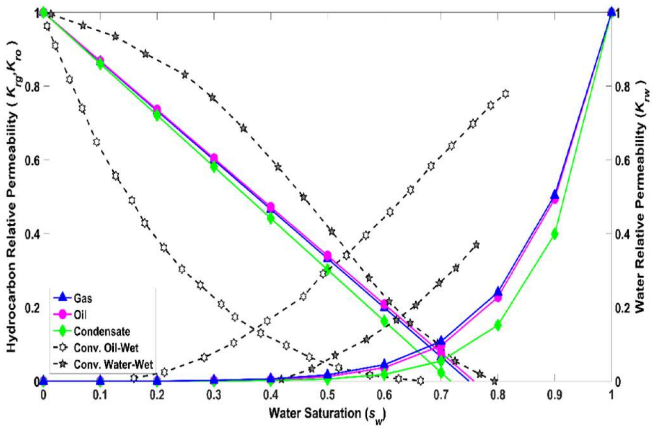

Figure 10 – Average relative permeability curves obtained from various shale samples (Ojha et al. 2017)

Based on Ojha et al.'s work (2017), a curve fitting process was conducted to fit the measurement data with the Stone II model (Stone, 1973; Chen, 2019) as shown in Figs. 11 and 12. By doing the fitting process, all the key parameters of the relative permeability curves in the Stone II model are defined as the base case in CMG and can be modified in the history matching process if necessary.

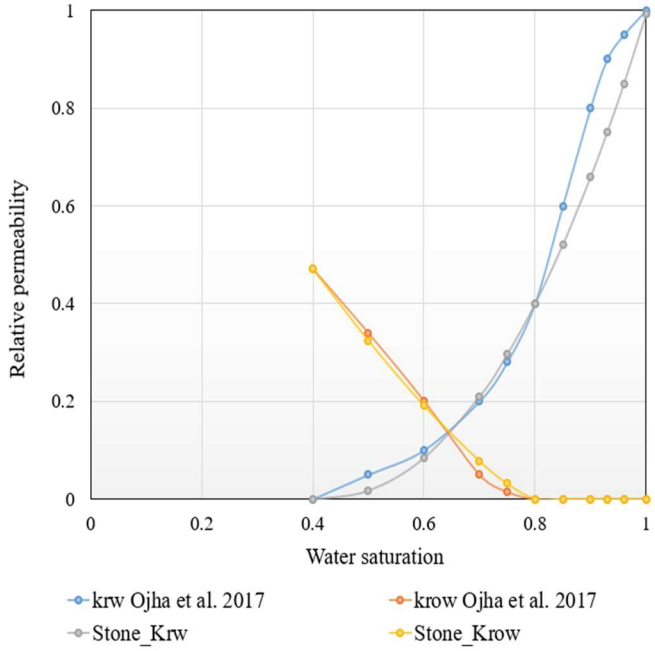

Figure 11 – Relative permeability curve fitting for water-oil system in Wolfcamp shale

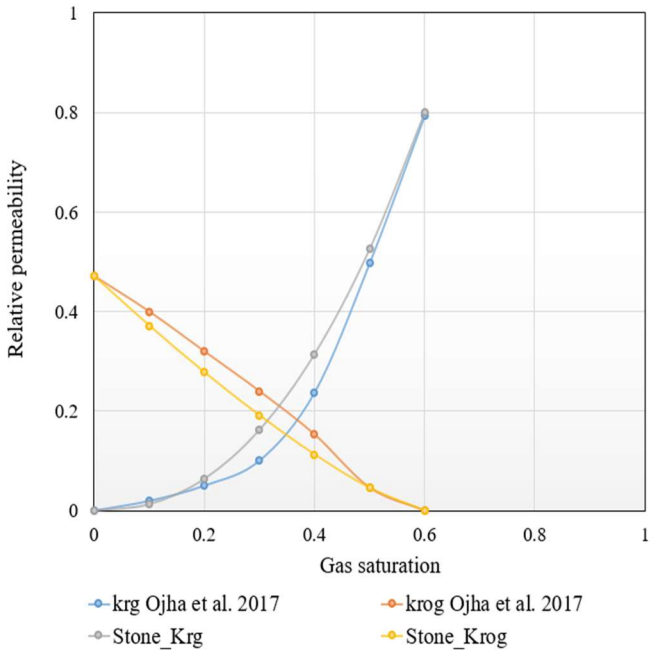

Figure 12 – Relative permeability curve fitting for gas-oil system in Wolfcamp shale

Results and discussion

Parent well fractures propagation

Based on the field data, the parent well was hydraulically fractured with 21 stages; injection rate and pumping time of each stage were 75 bpm and 106 minutes, respectively. Information about proppant type is not available; however, it is very common to use 100-mesh sand in the Wolfcamp formation in Delaware Basin, therefore, 100-mesh sand properties will be used in the simulation. It is also important to note that, the proppant permeability and hence the fracture conductivity is controlled by proppant type and closure stress. A 100-mesh sand with permeability of 10,000 mD at no-stress condition can be reduced to 2000 mD at 10,000 psi closure stress corresponding to a fracture conductivity of 60 to 8 mD-ft (Huang et al. 2019). If any of the realistic conditions are worse, then 100-mesh conductivity may be lower than 1.7 mD-ft due to unforeseen damage effects (Al-Tailji et al. 2016). The fracture propagation of the parent well was simulated by implementing the treatment schedule as stated above. The fundamental computation to create hydraulic fracture is presented in Step 3 of the workflow. Fig. 13 presents the fractures propagation of the parent well as well as permeability in millidarcy of the fracture system right after pumps shut. As shown in Fig. 13, fractures do not propagate symmetrically as described in the theoretical bi-wing planar fracture model. The fracture geometry of a certain stage is driven by the magnitude and direction of the current effective minimum horizontal stress, which is affected by the preceding stages. Thus, fracture half-length is in the range of 150 to 900 ft rather than being fixed at a certain value. Fracture height from the simulation results also varies from 100 to 400 ft. Fig. 14 shows the effective minimum horizontal map after fracturing of 21 stages to provide an insight into fractures' growth mechanism. As shown in Fig. 14,

fractures tend to avoid high stress region created by the previous stages. As a fracture initiates when tensile failure criterion satisfied, it adds an additional stress to the neighbouring zone at the same time. This additional stress is similar to the stress shadowing concept in some other publications (Dohmen et al. 2014; Ghassemi 2017; Roussel 2021). Since stress shadowing increases effective minimum horizontal stress, it makes the formation harder to be fractured. If the additional stress is high enough, it may cause fracture reorientation depending on the direction of the current minimum horizontal stress. In such cases, fractures will propagate in both transversal and longitudinal directions. Generally, operators want fractures to growth perpendicular to the wellbore, rather than propagating along the wellbore, to produce the most out of the formation.

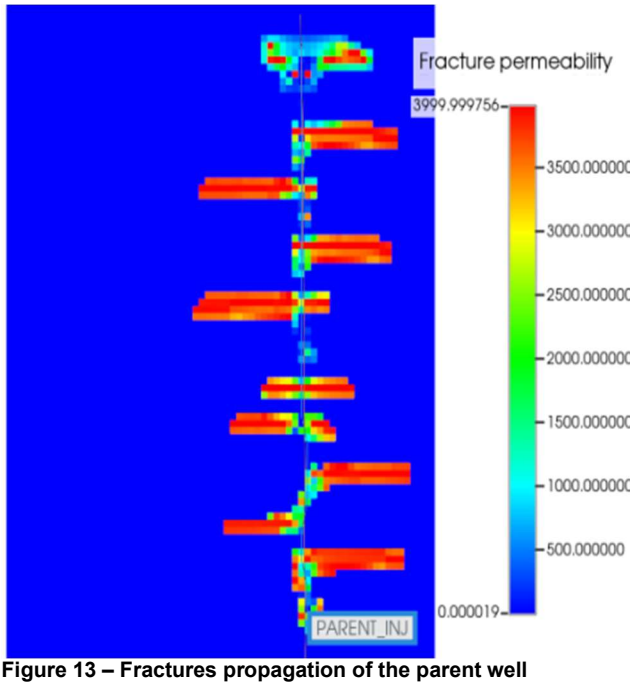

Figure 13 – Fractures propagation of the parent well

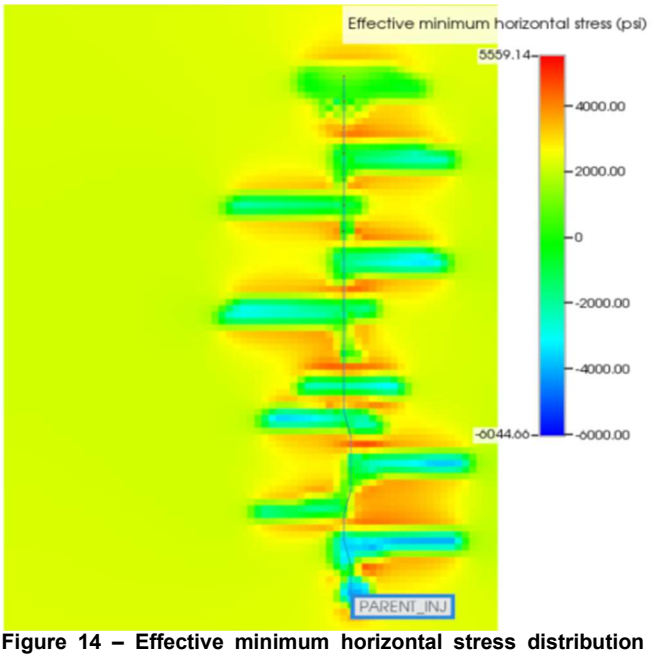

Figure 14 – Effective minimum horizontal stress distribution after hydraulic fracturing of the parent well

History matching production of parent well

To validate the quality of fracture simulation in previous section, the history matching was conducted using the available monthly production data of oil, gas, and water. The history matching process is conducted based on bottom hole pressure (BHP) control mode using CMOST-AI (an Intelligent Optimization and Analysis Tool in CMG).

The first step of the history matching is to perform sensitivity analysis to identify the most sensitive parameters to the oil, gas, and water productions. Since the reservoir properties, fluid properties, and well completion are based on field data, the most potential uncertainties are relative permeability in the fracture system, closure and residual fracture permeability. The sensitivity analysis was run with 10 uncertain parameters as shown in Table 2 as follows:

Table 2. Uncertain variables in history matching

Variables	Base values	Range of variations	
		Minimum	Maximum
Closure fracture permeability, mD	0.7	0.525	0.875
Residual fracture permeability, mD	0.25	0.1875	0.3125
KRGCL	0.9	0.7	1
KROCW	0.7	0.525	0.875
KROGCG	0.7	0.525	0.875
KRWIRO	0.7	0.525	0.875
NW	2	1	2.5
NOW	1	1	2
NG	1	1	2
NOG	1	1	2

Where KRGCL is gas relative permeability at connate liquid, KROCW is oil relative permeability at connate water, KROGCG is oil relative permeability at connate gas, KRWIRO is water relative permeability at irreducible oil, NW is curvature exponent of water curve in water-oil system, NOW is curvature exponent of oil curve in water-oil system, NG is curvature exponent of gas curve in gas-liquid system, NOG is curvature exponent of oil curve in gas-liquid system.

Tornado charts with the influence of each independent variable on oil, gas, and water cumulative production are shown in Figs. 15, 16, and 17, respectively. The charts give an insight into how each variable contributes to cumulative oil, gas, and water.

For example, in Fig. 15, combination effect of residual fracture permeability and curvature exponent of oil curve in water-oil system has negative effects on oil cumulative. This observation is understandable because a high exponent of oil curve causes a low oil flow compared with water flow in the water-oil system. Meanwhile, the residual permeability (under closure stress) itself has positive impact on the oil cumulative; increase of this variable will increase oil production. Clearly, the effects of closure and residual fracture permeability on cumulative oil production are significant and they play an important role in the history matching. The same interpretations are applied to cumulative gas and water production to obtain a better insight into the history matching process. With the understanding of how sensitive each parameter is, the production history matching can be achieved more conveniently.

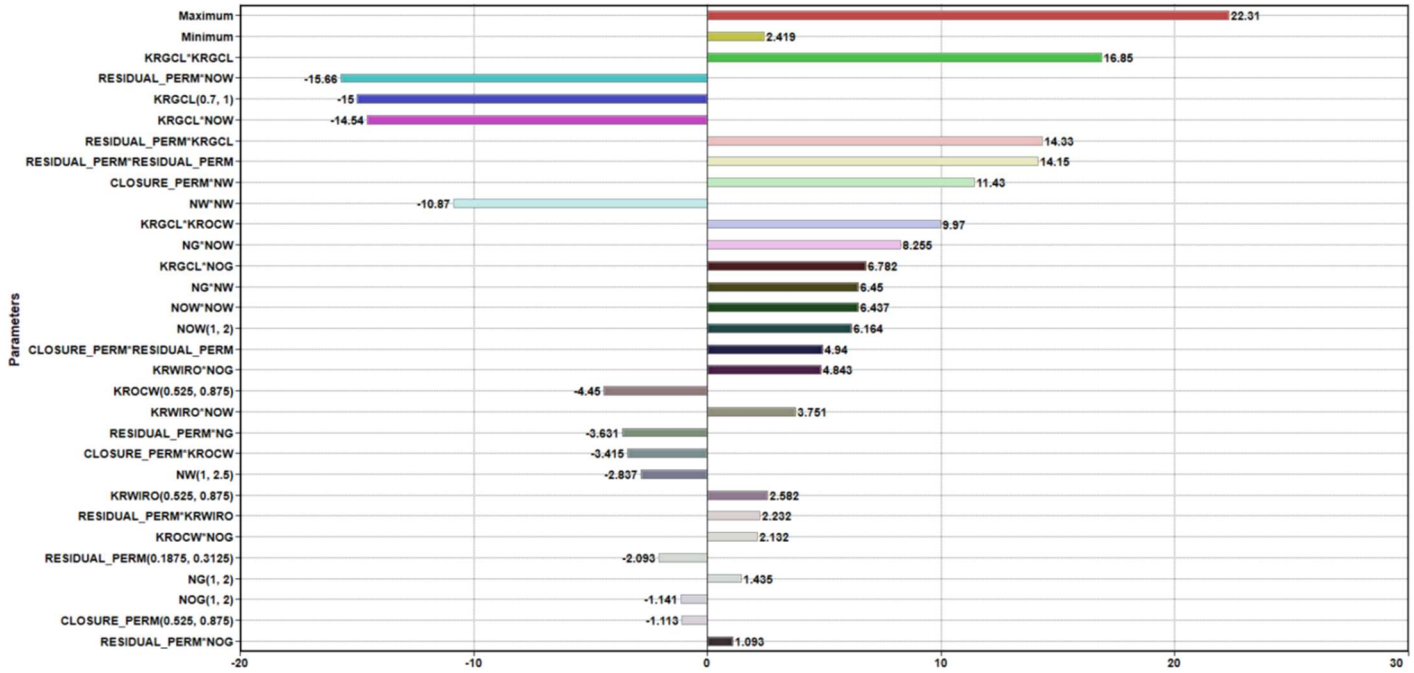

Figure 15 – Tornado chart analysis for the most sensitive parameter to cumulative oil production

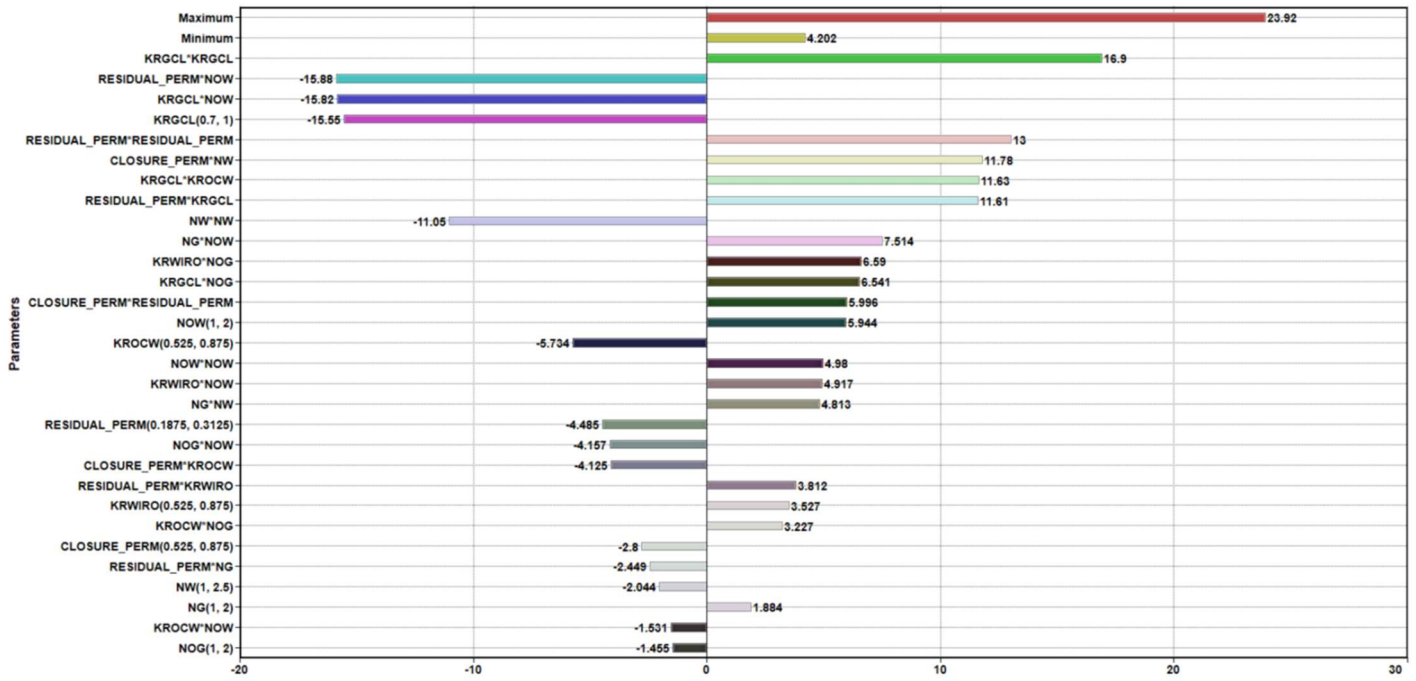

Figure 16 – Tornado chart analysis for the most sensitive parameter to cumulative gas production

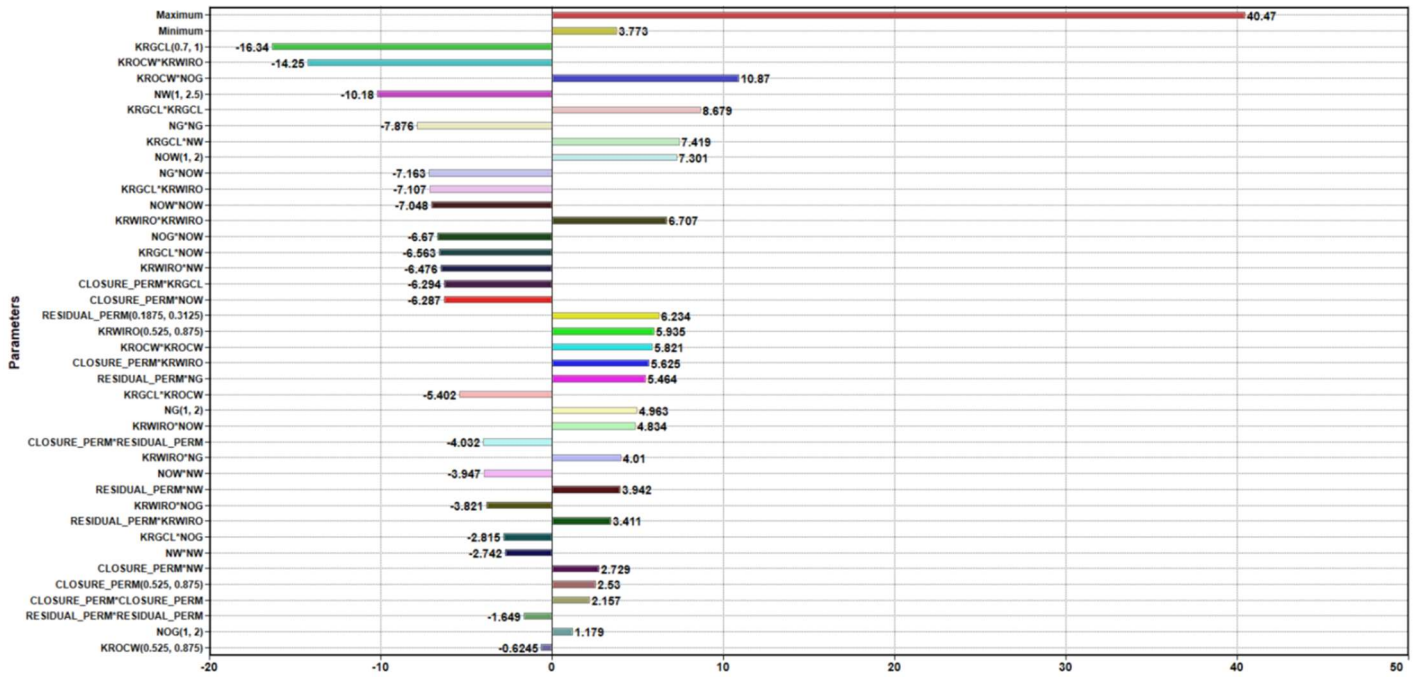

Figure 17 – Tornado chart analysis for the most sensitive parameter to cumulative water production

In the second step, CMOST-AI changes the individual parameters to reduce the difference between the simulated and observed production data. This process determines optimal output to imitate the observed data by systematically utilizing a combination of parameters in fracture permeability and relative permeability curves. The model ran through 200 iterations to obtain the most accurate model with a global error of 6.4%. Once the model was calibrated with data that matched the observed production, changes were made automatically by CMOST-AI inside the model to give an accurate representation of the fracture permeability and relative permeability curves in the fracture system. Figs. 18, 19, and 20 present the optimal solution of the history matching process for oil, gas, and water production of the parent well, respectively.

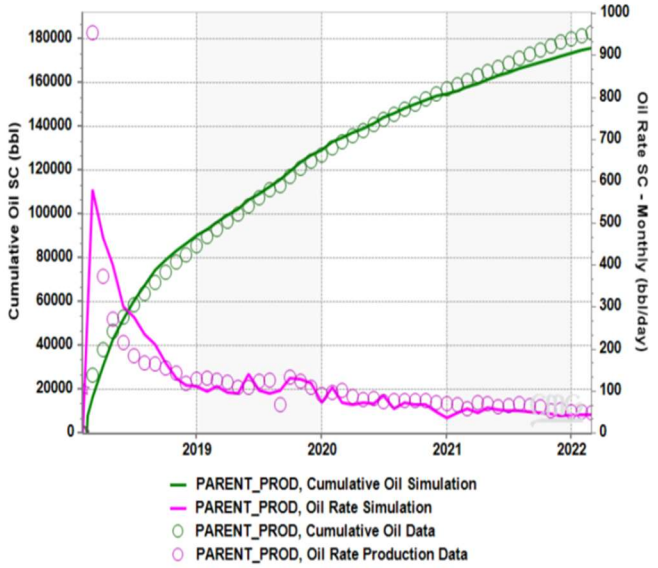

Figure 18 – History matching for oil production

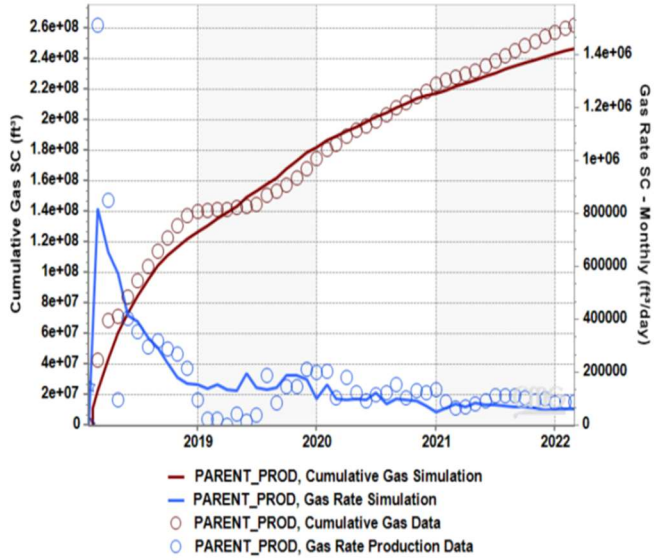

Figure 19 – History matching for gas production

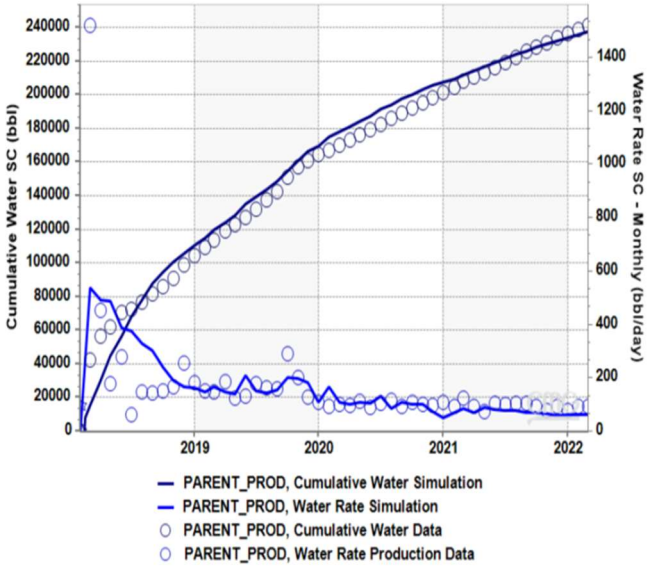

Figure 20 – History matching for water production

Well spacing analysis

After history matching, the model can be used as the representative for the formation of interest. The well spacing analysis between the parent well and a new infill well (child well) was conducted used the matched model. To reduce the uncertainties affecting on EUR, the child well is assumed to be parallel with the parent well and it is fractured with the same fracture treatment as the parent well (21 stages, 106 minutes pumping each stage, pump rate of 75 bpm, and 100-mesh sand). According to N.M. Code R. § 19.15.16.15, the distance in the horizontal plane from any point in the completed interval to any outer boundary of the horizontal spacing unit, measured along a line perpendicular to the completed interval or to the tangent thereof, shall be a minimum of 330 feet for an oil well or 660 feet for a gas well. Therefore, a minimum 660-ft spacing between two wells is applied. The common spacing in the Eddy County and Lea County for a four-well pad in one section covering an area of one mile-by-one mile is 1320 ft. Therefore, the spacing analysis was conducted from 600 to 1300 ft with 50-ft increment. The first case was run is the minimum 600-ft spacing, then a 50-ft spacing increment for each following cases until 1300-ft spacing were run. There are 15 cases total for the well spacing from 600 to 1300 ft to determine the optimal spacing that gives the highest EUR.

Fig. 21 shows the simulation result of the 600-ft spacing case after fracturing of the child well. As shown in Fig. 21, more than one stage of parent and child well connect together so they produce in the same stimulated zone. That is a clear evidence of well communication in this very close spacing case. Well communication or frac-hit are often the root causes of the low EUR but not always. To determine the optimal spacing, both wells are put in production five years after fracturing of the child well. The total production of both wells in 15 cases of different well spacing are shown in the scatter plot in Fig. 22 for comparison. The total production of cases from 600 to 900-ft spacing present very similar total production in five years.

Simulation results of fracture propagation provide a good explanation for this observation. As shown in Fig. 23 for the spacing of 900 ft, the fractures of child well still tend to move toward the fracture zone of the parent well. It means both wells are producing from an overlap stimulated zone so the performance is inefficient. Other cases from 600 to 900-ft spacing show the same observation and that is the reason for the very similar EUR of these cases. It is an evident example of detrimental impact of frac-hit on the cumulative production.

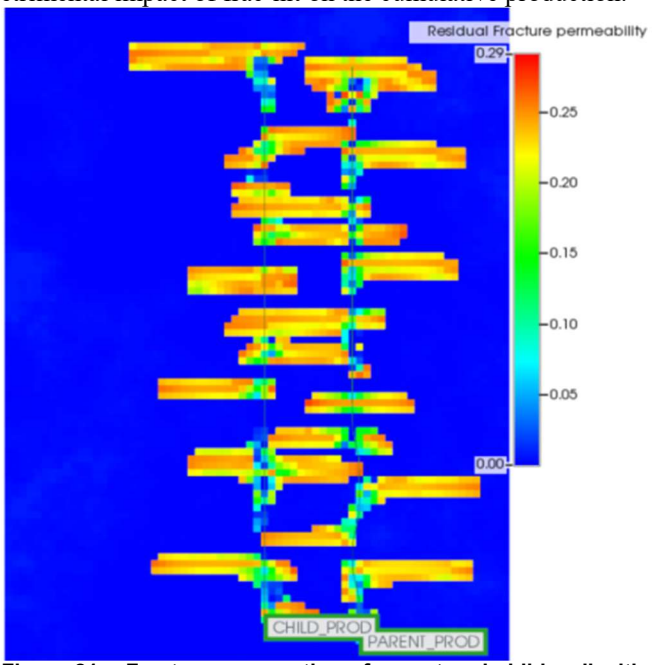

Figure 21 – Fracture propagation of parent and child well with 600-ft spacing

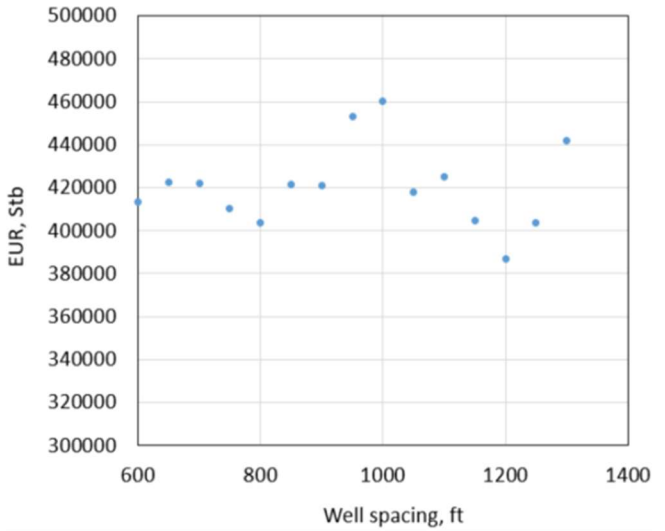

Figure 22 – Total production in 5 years versus well spacing

Out of the spacing range from 600 to 900 ft, the 1000-ft spacing case shows the highest EUR compared to the rest of cases as shown in Fig. 22. This is also understandable under the view of the child well's fracture propagation. Looking at the child well's fracture in Fig. 24, they start to move away from the overlap zone. Even if some fractures of the child well still communicate with the parent well, they do not grow too deep into the fractures of the parent well; therefore, they avoid producing from each other's stimulated area. In this way, both wells are able to produce the most hydrocarbon out of the middle oil bank and save the undisturbed formation for future development.

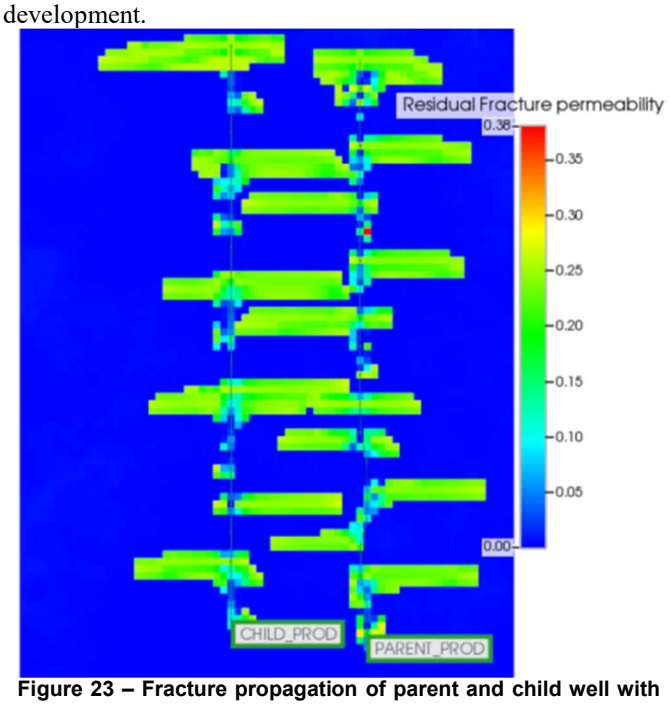

Figure 23 – Fracture propagation of parent and child well with 900-ft spacing

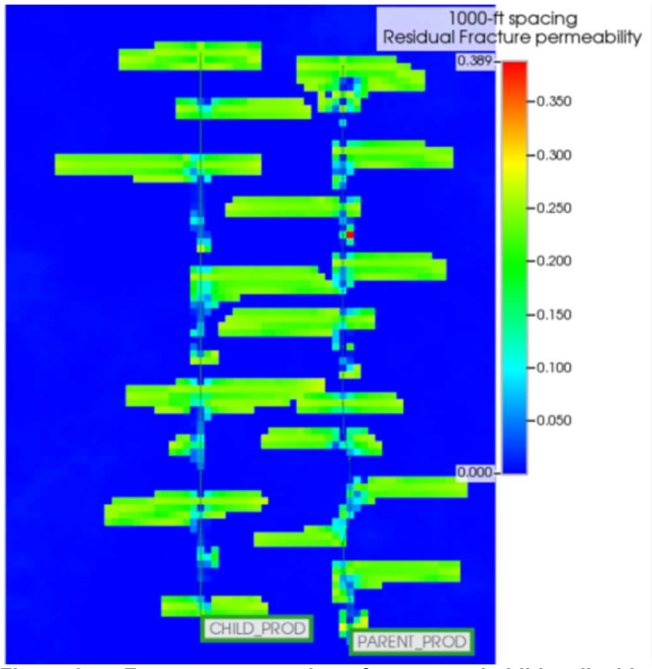

Figure 24 – Fracture propagation of parent and child well with 1000-ft spacing

However, spacings further than 1000 ft show a dramatic drop in total production of both well with the lowest EUR at 1200-ft spacing before raising up at the case of 1300-ft spacing.

This drop comes from the ineffective fracture job of the child well caused by the combined effect of formation heterogeneity and altered stress condition. Therefore, a considerable number of stages of the child well grow along the wellbore (longitudinal fractures). Obviously, these stages are not as effective as the transverse fractures. As mentioned above, additional stress created by the depletion of the parent well makes the rock more difficult to fracture. Once the fractures of the child well initiate along the wellbore, they keep growing in that direction because that is the least resistant path. In addition, since the reservoir is very heterogeneous as shown in Figs. 8 and 9, the production of the child well is also a function of reservoir quality and drilling location so the well spacing analysis also presents the best location giving highest production of the child well. Fig. 25 shows the fracture propagation of the child well for 1300-ft spacing for comparison with the 1000-ft case.

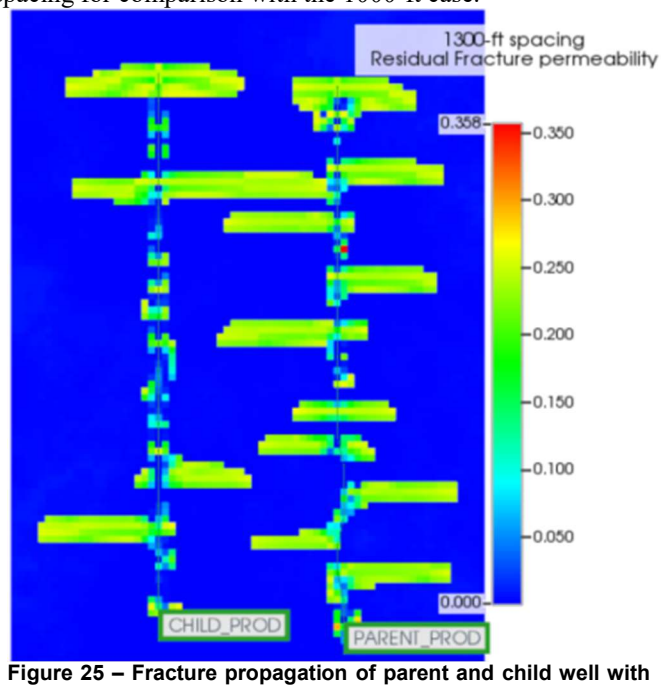

Figure 25 – Fracture propagation of parent and child well with 1300-ft spacing

By conducting the well spacing analysis, it is feasible to determine the optimal spacing between wells in the formation of interest and determine the location of the infill well that results in the highest EUR. Furthermore, the total production of a whole section is a function of well spacing and reservoir quality (porosity, permeability). This implies there will be an optimal spacing and drilling location of the child well for a specific formation. Therefore, the presented workflow can be applied to other formations of interest to determine the best area for the infill well development.

Conclusions

This paper presented a completed workflow to construct a numerical simulation to predict the optimal well spacing for the formation Wolfcamp A formation in the Delaware Basin in Lea County, New Mexico. Following this four-step workflow, one can estimate the optimal well spacing for other investigated formations.

Estimation of geological properties of the Wolfcamp A formation in Lea County through a MEM was provided including pore pressure, minimum horizontal and overburden stresses, as well as stress ratio between maximum and minimum horizontal stresses.

The CMOST-AI – optimization and analysis tool – provides a powerful tool for machine-learning-assisted history matching. The model could be run as many cases as needed to give an optimal solution that imitates the observed production data by changing sets of uncertainties.

The history match was then used for a well spacing analysis for the optimal spacing in the location of interest. In this particular case, an optimal spacing was determined of 1000 ft assuming the child well implements the same fracture treatment as the parent well. This means there could be five wells drilled in one section instead of four in a four-well pad as commonly implemented in the Delaware Basin. The well spacing analysis also reveals that total production is not only dependent well communication but also a function of child well's location and reservoir quality where it is drilled. Using this analysis process, one can determine the best location to drill the infill well to achieve the highest total recovery.

Acknowledgments

The authors wish to thank the Production and Drilling Research Project (PDRP) at New Mexico Tech (NMT) and Computer Modelling Group Ltd. for supporting the authors to accomplish this work.

Nomenclature

Define symbols used in the text here unless they are explained in the body of the text. Use units where appropriate.

A_φ	= *Faulting regime parameter*
GR_{index}	= *Gamma-ray index*
GR_{matrix}	= *Gamma-ray of a clean reservoir, gAPI*
GR_{shale}	= *Gamma-ray of a 100% shale zone, gAPI*
P_n	= *Normal hydrostatic pressure, psi*
P_p	= *Pore pressure, psi*
V_p	= *compressional velocity, ft/s*
V_{sh}	= *Volume of shale*
f_{rs}	= *Tensile stress, psi*
k_{hf}	= *Fracture permeability, mD*
k_{ccf}	= *Closure fracture permeability, mD*
k_{rcf}	= *Residual fracture permeability, mD*
ε_h	= *Minimum horizontal strain, ft/ft*
ε_H	= *Maximum horizontal strain, ft/ft*
ρ_b	= *Bulk density, g/cm^3*
ρ_f	= *Fluid density, g/cm3*
ρ_{ma}	= *Rock matrix, g/cm3*
ρ_{sh}	= *Density of shale, g/cm3*
σ_h	= *Minimum horizontal stress, psi*
σ_h'	= *Effective minimum horizontal stress, psi*
σ_H	= *Maximum horizontal stress, psi*
σ_V	= *Vertical stress, psi*
φ_N	= *Neutron porosity, ft^3/ft^3*

φ_T = *Total porosity, ft^3/ft^3*
φ_e = *Effective porosity, ft^3/ft^3*
φ_{sh} = *Shale porosity, ft^3/ft^3*
Δt_n = *Compressional slowness at normal pressure, µs/ft*
E = *Young's modulus, psi*
KRGCL = *Gas relative permeability at connate liquid*
KROCW = *Oil relative permeability at connate water*
KROGCG = *Oil relative permeability at connate gas*
KRWIRO = *Water relative permeability at irreducible oil*
n = *Eaton exponent*
NG = *Curvature exponent of gas curve in gas-liquid system*
NOG = *Curvature exponent of oil curve in gas-liquid system*
NOW = *Curvature exponent of oil curve in water-oil system*
NW = *Curvature exponent of water curve in water-oil system*
v = *Poisson's ratio*
k = *Rock matrix permeability, mD*
α = *Biot constant*
α, β = *Fitting parameters in Gardner's equation*

References

1. Alberty, M. 1994. "Standard interpretation: part 4 – wireline methods." D. Morton-Thompson and A. M. Woods, eds., Development Geology Reference Manual: AAPG Methods in Exploration Series 10, p. 180-185.
2. Al-Tailji, W.H., Shah, K., Davidson, B.M. 2016. "The Application and Misapplication of 100-mesh Sand in Multi-Fractured Horizontal Wells in Low-Permeability Reservoirs." SPE Hydraulic Fracturing Technology Conference, The Woodlands, Texas, February 9-11, 2016. SPE-179163-MS. https://doi.org/10.2118/179163-MS
3. Alzahabi, A., Kamel, A., Harouaka, A., Trindade A.A. 2021. "Optimal Spacing of the Wolfcamp in the Delaware Basin." Global Journal of Engineering Sciences, ISSN:2641-2039. https://doi.org/10.33552/GJES.2021.07.000663
4. Ampomah, W., Acheampong, S.A., McMillan, M., Bratton, T., El-Kaseeh, G. 2022. "Development of a Machine Learning Assisted Framwork in Calibrating In-Situ Stress Changes Through Time-lapse Vertical Seismic Profiling." 16th International Conference on Greenhouse Gas Control Technologies (GHGT-16), Lyon, France, October 23-24, 2022. https://ssrn.com/abstract=4285741
5. Bowers, G.L. 1995. "Pore Pressure Estimation From Velocity Data: Accounting for Overpressure Mechanism Besides Undercompaction." SPE Drilling & Comletion 10 (02): 89-95. SPE-27488-PA. https://doi.org/10.2118/27488-PA
6. Bradford, I.D.R., Fuller, J., Thompson, P.J., Walsgrove, T.R. 1998. "Benefits of Assessing the Solids Production Risk in a North Sea Reservoir Using Elastoplastic Modelling." SPE/ISRM Rock Mechanics in Petroleum Engineering, Trondheim, Norway, July 08, 1998. SPE-47360-MS. https://doi.org/10.2118/47360-MS
7. Bui, D., Nguyen, T., Nguyen, T., Yoo, H. 2022. "Formation damage simulation of a multi-fractured horizontal well in a tight gas/shale oil formation." Journal of Petroleum Exploration and Production Technology, 2022. https://doi.org/10.1007/s13202-022-01544-8.
8. Canady, W. 2011. "A Method for Full-Range Young's Modulus Correction." North American Unconventional Gas Conference and Exhibition, The Woodlands, Texas, June 14, 2011 SPE-143604-MS. https://doi.org/10.2118/143604-MS
9. Cao, R., Li, R., Girardi, A., Chowdhury, N., Chen, C. 2017. "Well Interference and Optimum Well Spacing for Wolfcamp Development at Permian Basin." SPE/AAPG/SEG Unconventional Resources Technology Conference, Austin, Texas, July 24-26, 2017. URTEC-2691962-MS. https://doi.org/10.15530/URTEC-2017-2691962
10. Cipolla, C.L., Williams, M.J., Weng, X., Mack, M., Maxwell, S. 2010. "Hydraulic fracture monitoring to reservoir simulation: maximizing value." Second EAGE Middle East Tight Gas Reservoir Workshop. https://doi.org/10.3997/2214-4609.20145655
11. Coates, G.R., Denoo, S.A. 1981. "Mechanical Properties Program Using Borehole Analysis And Mohr's Circle." SPWLA 22nd Annual Logging Symposium, Mexico City, Mexico, June 23, 1981. SPWLA-1981-DD.
12. Dohmen, T., Zhang, J., Blangy, J.P. 2014. "Measurement and Analysis of 3D Stress Shadowing Related to the Spacing of Hydraulic Fracturing in Unconventional Reservoirs." SPE Annual Technical Conference and Exhibition, Amsterdam, The Netherlands, October 27, 2014. SPE-170924-MS. https://doi.org/10.2118/170924-MS
13. Dvory, N.Z., Zoback, M.D. 2021. "Prior oil and gas production can limit the occurrence of injection-induced seismicity: A case study in the Delaware Basin of western Texas and southeastern New Mexico, USA." The Geological Society of America. https://doi.org/10.1130/G49015.1
14. Eaton, B.A. 1975. "The Equation for Geopressure Prediction from Well Logs." SPE-5544-MS. https://doi.org/10.2118/5544-MS
15. Ghassemi, A. 2017. "Application of rock failure simulation in design optimization of the hydraulic fracturing." Porous Rock Fracture Mechanics, Woodhead Publishing, 2017, P. 3-23. ISBN 9780081007815. https://doi.org/10.1016/B978-0-08-100781-5.00001-4
16. Hefner, W. 2020. "Case Study: Integrated Core Modeling and Simulation of Unconventional Hydraulically Fractured Wells in the Delaware Basin." OU – Theses [1862]. https://hdl.handle.net/11244/324843
17. Hefner, W., Davudov, D. 2019. "Field Development Using Compositional Reservoir Simulation and Uncertainty Analysis in the Delaware Basin." SPE Oklahoma City Oil and Gas Symposium, Oklahoma City, Oklahoma, April 9-10, 2019. SPE-195239-MS. https://doi.org/10.2118/184426-MS
18. Huang, J., Safari, R., Perez, O., Fragachan, F.E. 2019. "Reservoir Depletion-Induced Proppant Embedment and Dynamic Fracture Closure." SPE Middle East Oil and Gas Show and Conference, Manama, Bahrain, March 15, 2019. SPE-195135-MS. https://doi.org/10.2118/195135-MS
19. Jones, R.Z. 2019. "Nanopetrophysical Characterization of the Wolfcamp A Shale Formation in the Permian Basin of Southeastern New Mexico, U.S.A." ProQuest Number: 27805361. https://hdl.handle.net/10106/28841
20. Khodabakhshnejad, A. 2019. "Impact of Frac Hits on Production Performance – A Case Study in Marcellus Shale." SPE Western Regional Meeting, San Joe, California, April 23-26, 2019. SPE-195296-MS. https://doi.org/10.2118/195296-MS
21. King, G.E., Rainbolt, M.F., Swanson, C. 2017. "Frac Hit Induced

Production Losses: Evaluating Root Causes, Damage Location, Possible Prevention Methods and Success of Remedial Treatments." SPE Annual Technical Conference and Exhibition, San Antonio, Texas, October 9-11, 2017. SPE-187192-MS. https://doi.org/10.2118/187192-MS

22. Koray, A., Bui, D., Ampomah, W., Appiah-Kubi, E., Klumpenhower, J. 2023b. "Improving Subsurface Characterization Utilizing Machine Learning Techniques." SPE Western Regional Meeting, Anchorage, Alaska, May 21-23, 2023. SPE-212952-MS.
23. Koray, A., Bui, D., Ampomah, W., Appiah-Kubi, E., Klumpenhower, J. 2023a. "Application of Machine Learning Optimization Workflow to Improve Oil Recovery." SPE Oklahoma City Oil and Gas Symposium, Oklahoma City, Oklahoma, April 17-21, 2023. SPE-213095-MS.
24. Lehmann, J., Budge, J., Palghat, A., Petr, C., Pyecroft, J. 2016. "Expanding Interpretation of Interwell Connectivity and Reservoir Complexity through Pressure Hit Analysis and Microseismic Integration." SPE Hydraulic Fracturing Technology Conference, The Woodlands, Texas, February 01, 2016. SPE-179173-MS. https://doi.org/10.2118/179173-MS
25. Liang, B., Du, M., Goloway, C., Hammond, R., Yanez, P.P., Tran, T. 2017. "Subsurface Well Spacing Optimization in the Permian Basin." SPE/AAPG/SEG Unconventional Resources Technology Conference, Austin, Texas, July 24-26, 2017. https://doi.org/10.15530/URTEC-2017-2671346
26. Liang, B., Khan, S., Tang, Y. 2017. "Fracture Hit Monitoring and Its Mitigration Through Integrated 3D Modeling in the Wolfcamp Stacked Pay in the Midland Basin." SPE/AAPG/SEG Unconventional Resources Technology Conference, Austin, Texas, July 24, 2017. URTEC-2671336-MS. https://doi.org/10.15530/URTEC-2017-2671336
27. Luo, M., Baker, M.R., LeMone, D.V. 1994. "Distribution and Generation of the Overpressure System, Eastern Delaware Basin, Western Texas and Southern New Mexico." AAPG Bulletin, V. 78, No. 9 (September 1994), P. 1386–1405.
28. McKenna, J., Grealy, M., Blaz, M., Toohey, N. 2016. "Using depletion-zone microseismicity to understand producing volumes." SEG Technical Program Expanded Abstract 2016 (pp. 5043-5047). Society of Exploration Geophysicists. https://doi.org/10.1190/segam2016-13779054.1
29. Michael, A. 2022. "Guest Editorial: Four Real-World Challenges in Hydraulic-Fracture Modelling." Journal of Petroleum Technology 74 (08): 8 – 11. SPE-0822-0008-JPT. https://doi.org/10.2118/0822-0008-JPT
30. Morales, R.H., Marcinew, R.P. 1993. "Fracturing of High-Permeability Formations: Mechanical Properties." SPE 68th Annual Technical Conference and Exhibition, Houston, Texas, October 3-6, 1993. SPE-26561-MS. https://doi.org/10.2118/26561-MS
31. Neuhaus, C.W., McKenna, J., Zeynal, A.R., Telker, C., Ellison, M. 2014. "Completions and reservoir engineering applications of microseismic data." SEG Technical Program Expanded Abstracts 2014 (pp. 4564-4569). Society of Exploration Geophysicists. https://doi.org/10.1190/segam2014-1365.1
32. Nguyen, S.T., Hoang, S.K., Khuc, G.H. 2018. "Improved Pre-Drill Pore Pressure Prediction for HPHT Exploration Well Using 3D Basin Modelling Approach, A Case Study Offshore Vietnam." OTC-28606-MS, Offshore Technology Conference Asia, Kuala Lumpur, Malaysia, March 20-23, 2018. https://doi.org/10.4043/28606-MS.
33. Nguyen, S.T., Hoang, S.K., Khuc, G.H., Tran, H.N. 2015. "Pore Pressure and Fracture Gradient Prediction for the Challenging High Pressure and High Temperature Well, Hai Thach Field, Block 05-2, Nam Con Son Basin, Offshore Vietnam: A Case Study." SPE/IATMI Asia Pacific Oil & Gas Conference and Exhibition, Nusa Dua, Bali, Indonesia, October 20-22, 2015. SPE-176276-MS. https://doi.org/10.2118/176276-MS
34. Nguyen, S.T., Nguyen, T.C., Yoo, H., El-kaseeh, G., Eales, M. 2023. "Geomechanical Study and Wellbore Stability Analysis for Potential CO2 Storage into Devonian and Silurian Formation of Delaware Basin." 2023 SPE OKC Oil and Gas Symposium. SPE-213073-MS.
35. Nguyen, T.C., Pande, S., Bui, D., Al-Safran, E., Nguyen, H.V. 2020. "Pressure dependent permeability: Unconventional approach on well performance." Journal of Petroleum Science and Engineering 193 (2020) 107358. https://doi.org/10.1016/j.petrol.2020.107358
36. Ojha, S.P., Misra, S., Tinni, A., Sondergeld, C., Rai, C. 2017. "Relative permeability estimates for Wolfcamp and Eagle Ford shale samples from oil, gas and condensate windows using adsorption-desorption measurements." Fuel 208 (2017) 52-64. https://dx.doi.org/10.1016/j.fuel.2017.07.003
37. Park, J., Janova, C. 2020. "Stimulated Reservoir Volume Characterization and Optimum Lateral Well Spacing Study of Two-Well Pad: Midland Basin Case Study." Geofluids 2020(9):1-18. http://doi.org/10.1155/2020/8829015.
38. Plumb, R.A. 1994. "Influence of compostition and texture on the failure properties of clastic rocks." Rock Mechanics in Petroleum Engineering, Delft, Netherlands, August 29, 1994. SPE-28022-MS. https://doi.org/10.2118/28022-MS
39. Ramiro-Ramirez, S., Bhandari, A.R., Flemings, P.B., Reed, R.M., 2020. "Porosity and Permeability Heterogeneity in the Upper Wolfcamp, Delaware Basin, West Texas: Implications for Production." SPE/AAPG/SEG Unconventional Resources Technology Conference, Virtual, July 20, 2020. https://doi.org/10.15530/URTEC-2020-2105
40. Rezaei, A., Dindoruk, B. Soliman, M.Y. 2019. "On parameters affecting the propagation of hydraulic fractures from infill wells." Journal of Petroleum Science and Engineering 182 (2019) 106255. https://10.1016/j.petrol.2019.106255
41. Roussel, N.P. 2017. "Analyzing ISIP Stage-by-Stage Escalation to Determine Fracture Height and Horizontal-Stress Anisotropy." SPE Hydraulic Fracturing Technology Conference and Exhibition, The Woodlands, Texas, January 24, 2017. SPE-184865-MS. https://doi.org/10.2118/184865-MS
42. Sani, A.M., Podhoretz, S.B., Chambers, B.D. 2015. "The Use of Completion Diagnostics in Haynesville Shale Horizontal Wells to Monitor Fracture Propagation, Well Communication, and Production Impact." SPE/CSUR Unconventional Resources Conference Calgary, Alberta, Canada, October 20, 2015. SPE-175917-MS. https://doi.org/10.2118/175917-MS
43. Snee, J.E.L., Zoback, M.D. 2018. "State of stress in the Permian Basin, Texas and New Mexico: Implications for induced seismicity." The Leading Edge (2018) 37 (2): 127-134. https://doi.org/10.1190/tle37020127.1
44. Tran, D., Buchanan, L., Nghiem, L. 2008. "Improved Gridding Technique for Coupling Geomechanics to Reservoir Flow." SPE Annual Technical Conference and Exhibition, Denver, Colorado, September 21-24, 2008. SPE-115514-MS. https://doi/org/10.2118/115514-MS
45. Tran, D., Nghiem, L., Buchanan, L. 2009a. "Aspects of Coupling Between Petroleum Reservoir Flow and Geomechanics." Asheville 2009, the 43rd US Rock Mechnics Symposium and 4th U.S.-Canada Rock Mechanics Symposium, Asheville, NC, June 28, 2009. ARMA 09-089.

46. Tran, D., Shrivastava, V., Nghiem, L., Kohse, B. 2009b. "Geomechanical Risk Mitigation for CO_2 Sequestration in Saline Aquifers." SPE Annual Technical Conference and Exhibition, New Orleans, Louisiana, October 4-7, 2009. SPE-12567-MS. https://doi.org/10.2118/125167-MS
47. Trowbridge, S., Wicker, J., Courtier, J., Fairfield, R., Campbell, T. 2017. "Application of Mircoseismic to Assess Hydraulic Fracture Behavior in Relation to Completion Design and Landing Zone." Unconventional Resources Technology Conference, Austin, Texas, July 24-26, 2017 (pp. 2017-2027). Society of Exploration Geophysicists, American Association of Petroleum Geologists, SPE. URTEC-2674376-MS. https://doi.org/10.15530/URTEC-2017-2674376
48. U.S. Energy Information Administration. Wolfcamp, Bone Spring, Delaware Shale Plays of the Delaware Basin, 2020. Available from www.eia.gov
49. Xiong, H., Wu, W., Gao, S. 2018. "Optimizing Well Completion Design and Well Spacing with Integration of Advanced Multi-Stage Fracture Modelling & Reservoir Simulation – A Permian Basin Case Study." SPE Hydraulic Fracturing Technology Conference & Exhibition, The Woodlands, Texas, January 3-25, 2018. SPE-189855-MS. https://doi.org/10.2118/189855-MS
50. Zhu, J., Forrest, J., Xiong, H., Kianinejad, A. 2017. "Cluster Spacing and Well Spacing Optimization Using Multi-Well Simulation for the Lower Spraberry Shale in Midland Basin." SPE Liquids-Rich Basins Conference – North America, Midland, Texas, September 13-14, 2017. SPE-187485-MS. https://doi.org/10.2118/187485-MS